# Portable 4D Snapshot Hyperspectral Imager for Fastspectral and Surface Morphology Measurements

**Jing Luo[1], Zijian Lin[1], Yuxin Xing[1], Erik Forsberg[1], Chengdong Wu[1], Xinhua Zhu[2], Tingbiao Guo[1], Gaoxuan Wang[1], Beilei Bian[3], Dun Wu[4], and Sailing He[1, \*]**

(*Invited Paper*)

**Abstract**—A portable 4D snapshot hyperspectral imager (P4DS imager) with compact size, fast imaging time, low cost, and simple design is proposed and demonstrated. The key components of the system are a projector, a liquid crystal tunable filter (LCTF), and a camera. It has two operating modes depending on the set state of the LCTF: a 3D light measurement mode that produces a 3D point cloud reconstruction of an object and a hyperspectral imaging mode yielding spectral data. The camera imaging plane is the same for both operating modes allowing the collected spatial and spectral data to be directly fused into a 4D data set without post-processing. The P4DS imager has excellent performance with a spectral resolution of 10 nm, a spatial depth accuracy of 55.7 μm, and a total 4D imaging time of 0.8 s. 4D imaging experiments of three different samples, namely, a colored figurine, green broccoli, and a human face, are presented to demonstrate the efficiency and applicability of the system. Due to being cost-effective, portable, and good imaging performance, the proposed system is suitable for commercialization and mass production.

## 1. INTRODUCTION

Hyperspectral imaging (HSI) is a powerful technology for molecular identification [1]. Using HSI, spectral information such as wavelength-dependent optical absorption intensity, $I$, can be recorded and assigned to a specific spatial location, i.e., to a corresponding pixel $(x, y)$ in a two-dimensional (2D) image, generating a corresponding hyperspectral cube $(x, y, I)$ [2, 3]. Due to its ability to spatially discriminate physicochemical properties with high accuracy, HSI has a broad range of application areas, e.g., quality control of food products [4, 5], geological remote sensing [6, 7], measurement of skin conditions [8, 9], and in a variety of biology studies [10, 11]. Depending on the scanning mode, common methods for HSI data acquisition can be categorized into three types: point-scanning [12], line-scanning [13], plane-scanning [14]. Among them, plane-scanning imagers, which typically use filters as the dispersive element, can capture multiple spectral images at one time. This type of hyperspectral imagers usually have a faster frame rate and perform well in multi-sensors systems [15–18].

Three-dimensional (3D) surface imaging can provide detailed depth information of the object under measurement, reflecting size, depth, detailed texture, and microscopic defects. Based on the optical imaging principle of choice, 3D imaging techniques can be classified into categories such as binocular vision [19, 20], structured illumination [21, 22], time of flight (TOF) [23], and LIDAR [24]. They have

different specific advantages in 3D spatial resolution, measurement distance, imaging time, and field-of-view (FOV) levels. As a result, 3D surface imaging techniques have been applied to a diverse set of applications in fields such as industrial inspection [25], cultural heritage documentation [26], 3D scene reconstruction [27], and real-time 3D imaging in consumer products [28].

As 3D imaging and HSI provide two pertinent types of information related to intrinsic properties that are key metrics for substance identification and analysis, it is highly beneficial to combine spectral information with a 3D reconstructed model to a unified four-dimensional (4D) data set $(x, y, z, I)$. Such higher-dimensional optical imaging systems, typically referred to as 4D imagers, have been studied extensively in laboratory settings [29–34]. Most previous 4D systems combine one of the HSI and one of the 3D reconstruction techniques mentioned above to achieve 4D imaging. During system design, the choice and matching of the two techniques are obviously crucial for the system performance, such as spatial and spectral resolution, fusion precision, and imaging time. A straightforward approach is to use a 3D imager and a hyperspectral sensor that separately collect spatial and spectral data as done by Ivorra et al., who utilized a 3D structured light system combined with a hyperspectral short-wave near-infrared system to estimate the freshness of gilthead sea bream [35]. However, as the two systems were not integrated but worked separately, one-to-one correspondence between the 3D and spectral data could not be established. Kim et al. reported a 3D scanning system that incorporated hyperspectral imaging, which was composed of a laser scanning 3D imager and a compressive sensing hyperspectral imager [36]. In this case, the compressive sensing method required high computational complexity, and fusion precision was relatively low as the two modules had no corresponding relationship. Chen et al. developed a hyperspectral LIDAR for point cloud segmentation, which was composed of a TOF measurement system and a galvanometer-based line-scan hyperspectral imager [37]. This system suffered from low spatial accuracy, long imaging time, and low density of the reconstructed point cloud. Recently, Li et al. reported a 4D line-scan hyperspectral imager based on structured light stereovision and line-scan hyperspectral imaging [38]. As only a single line-scan hyperspectral grayscale camera was utilized for the 3D image acquisition and the hyperspectral imaging, the performance of the 3D light structure stereovision was poor, being limited by the line-scanning mode, with a low spatial resolution and a time-consuming measurement process as a result. Most previously reported hyperspectral imaging systems are in addition bulky and have a relatively high manufacturing cost. However, taking practical applications and commercialization into account, portability and low cost are also important factors to be considered in the system design of a 4D imaging system.

In this paper, we report a portable 4D snapshot hyperspectral imager (P4DS imager) that combines a 3D measurement (with high depth accuracy) with hyperspectral imaging. The principal components of the system are a projector, a liquid crystal tunable filter (LCTF) with a 450–750 nm transmission wavelength range, and a grayscale camera. In the 3D measurement mode, structured light stripes with different frequencies and phases are projected on the target by the projector that, after being passed through the LCTF, are captured by the camera one by one for fast 3D reconstruction. The transmission band of the LCTF is set to be consistent with the wavelength of the projection light. Subsequently, the LCTF works in hyperspectral imaging mode, in which a controller is used to sweep the transmission wavelength over the 450–750 nm range. Monochrome images of the target at different wavelengths are collected by the camera. As the 3D and hyperspectral imaging share the same camera plane, the spatial and spectral data can directly be fused into a 4D data set without post-processing. The depth and spectral resolutions of the system are 55.7 µm and 10 nm, respectively, with an imaging time of less than 1 second. The system size is 20 cm * 25 cm * 10 cm, i.e., very compact and thus easily made portable. Owing to its simple design, low cost, small size as well as good imaging performance, the P4DS imager presented in this paper is well suited for commercialization.

The paper is structured as follows: Section 2 introduces the principles of operation of the hyperspectral snapshot imager and the structured light stereo vision. Section 3 does the same for the full proposed P4DS imager and also details performance tests that were carried out. In Section 4, three demonstration experiments with a colored figurine, a green plant and a human face as imaging objects are presented to demonstrate the performance of the P4DS imager and to substantiate the system's efficiency and applicability. The paper ends with a summary in Section 5.

## 2. METHODS

### 2.1. Hyperspectral Snapshot Imager

The hyperspectral snapshot imager consists of a liquid crystal tunable filter (LCTF) and a camera. The transmission wavelength of the LCTF is changed through electrical modulation, allowing the camera, which is placed behind the LCTF, to collect monochrome images corresponding to specific wavelengths so as to realize hyperspectral imaging. The principle of the transmission wavelength modulation of the LCTF is described in the following. Fig. 1(a) shows the basic structure of a single-stage Lyot filter [39], which consists of two parallel polarizers and a liquid crystal phase retarder with thickness $d$ and birefringent refractive index difference (for the two polarizations) $\Delta n$. Light with wavelength $\lambda$ acquires a phase delay $\Gamma$ when passing through the single-stage Lyot filter. The transmissivity $T$ of a single-stage Lyot filter $i$ can be expressed as [39]:

$$T = \frac{1}{2}\left(\cos\frac{\Gamma_i}{2}\right)^2 = \frac{1}{2}\left(\cos\frac{\pi\Delta nd_i}{\lambda}\right)^2 \tag{1}$$

Liquid crystals have an electrically controllable birefringence [40]. Applying bias voltages of different intensity on the parallel polarizers affect the molecular orientation of the liquid crystal, which alters the birefringent refractive index difference $\Delta n$ and, in turn, the phase delay $\Gamma$. Thus, as the wavelength transmissivity $T$ of a single-stage Lyot filter is determined by the phase delay $\Gamma$, electrical modulation of the transmissivity can be realized. The structure of a multistage Lyot filter (where each stage of the filter is twice as thick as the previous one) is shown in Fig. 1(b). The transmissivity of the multistage Lyot filter can be expressed as [39]:

$$T = \frac{1}{2}\prod_{i=1}^{N}\left(\cos\frac{2^{i-1}\Gamma_1}{2}\right)^2 = \frac{1}{2}\left[\frac{\sin\left(2^{N-1}\Gamma_1\right)}{2^N\sin\left(\Gamma_1/2\right)}\right]^2 \tag{2}$$

From Eq. (2), we see that the LCTF, which is composed of a multistage Lyot filter, has a single wavelength transmission peak, with transmission at other wavelengths being close to zero. By adjusting the bias voltage, the phase delay of the liquid crystal can be changed, shifting the transmission peak position. Fig. 1(c) shows the LCTF transmission curve modulated to different central wavelengths.
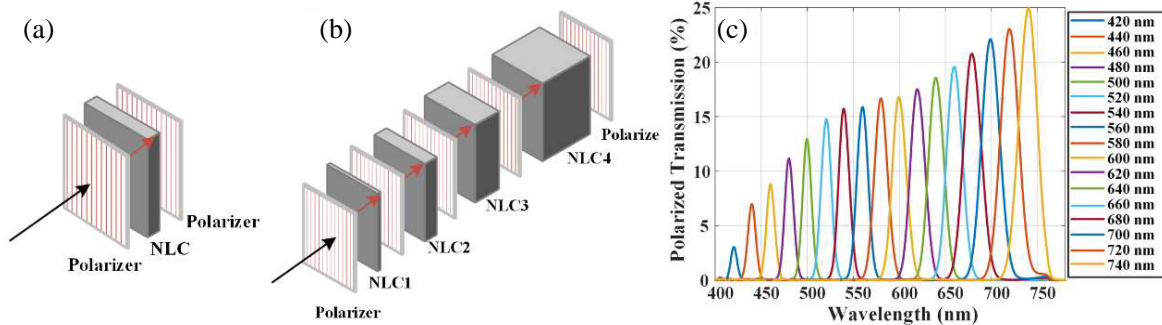


**Figure 1.** Structure of (a) a single-stage Lyot filter and (b) a multistage Lyotfilter. (c) Transmissivity curves of the LCTF for varying wavelengths.

### 2.2. Structured Light 3D Reconstruction

The 3D coordinates of the object under investigation are obtained using a plane structured light stereo vision system in which point coordinates are determined by triangulating the corresponding camera and projector pixels of the same object point in a setup as illustrated in Fig. 2. Structured light stripes at a specific frequency are projected on the object by a projector. The intensity of the structured light
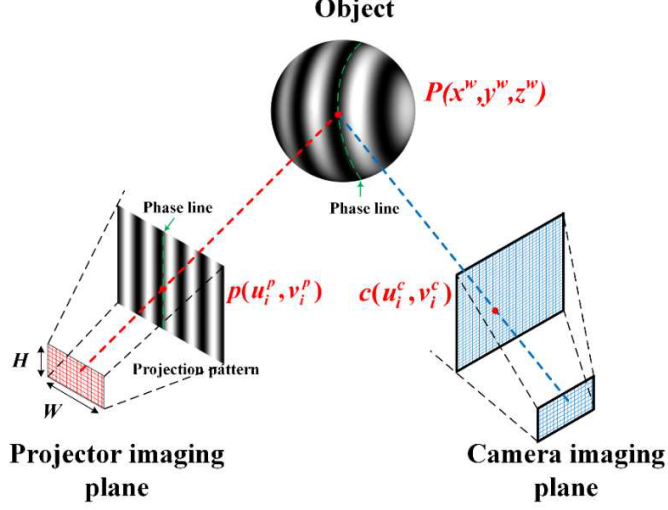
**Object**

$P(x^w,y^w,z^w)$

Phase line                     Phase line

$p(u_i^p,v_i^p)$    $c(u_i^c,v_i^c)$

$H$

Projection pattern

$W$

**Projector imaging**              **Camera imaging**
**plane**                               **plane**

**Figure 2.** Schematic of the structured light 3D reconstruction process.

stripes imaged at the camera plane is [41]:

$$I_m = \frac{1}{2} + \frac{1}{2} \times \cos(\varphi(u_i^c, v_i^c) + 2m\pi/4) \tag{3}$$

where $m$ is the phase-shifting step number, $(u_i^c, v_i^c)$ the pixel coordinate in the camera plane, and $\varphi(u_i^c, v_i^c)$ the relative phase of pixel $(u_i^c, v_i^c)$. According to the four-step phase-shift method [41], the relative phase $\varphi(u_i^c, v_i^c)$ can be calculated from Eq. (3) to be:

$$\varphi(u_i^c, v_i^c) = -\tan^{-1}\left[\frac{\sum\limits_{m=0}^{3} I_m \sin(2m\pi/4)}{\sum\limits_{m=0}^{3} I_m \cos(2m\pi/4)}\right] \tag{4}$$

Using the multi-wavelength heterodyne phase unwrapping solution [42], the periodic relative phase $\varphi(u_i^c, v_i^c)$ of a certain pixel in the projector plane can be transformed to an absolute phase value $\Phi_{ch}(u_i^c, v_i^c)$ in the horizontal direction and $\Phi_{cv}(u_i^c, v_i^c)$ in the vertical direction. Following this, the projector pixel coordinate $p(u_i^p, v_i^p)$ corresponding to the camera pixel $c(u_i^c, v_i^c)$ can be calculated to be:

$$u_i^p = \frac{\Phi_{ch}(u_i^c, v_i^c)}{2\pi} \times W \tag{5a}$$

$$v_i^p = \frac{\Phi_{cv}(u_i^c, v_i^c)}{2\pi} \times H \tag{5b}$$

where $W$ and $H$ are the width and height of the pixel image in the projector imaging plane. The light paths in front of both the camera and projector planes can be approximated by a pinhole camera model. Therefore, the correspondence of pixel coordinates $c(u_i^c, v_i^c)$ and $p(u_i^p, v_i^p)$ in the camera and projector imaging planes and the corresponding 3D coordinate $P(x^w, y^w, z^w)$ of the point on the object surface can be described as [42]:

$$z_c \begin{bmatrix} u_i^c \\ v_i^c \\ 1 \end{bmatrix} = K_c M_c \begin{bmatrix} x^w \\ y^w \\ z^w \\ 1 \end{bmatrix} \tag{6a}$$

$$z_p \begin{bmatrix} u_i^p \\ v_i^p \\ 1 \end{bmatrix} = K_p M_p \begin{bmatrix} x^w \\ y^w \\ z^w \\ 1 \end{bmatrix} \tag{6b}$$

where $K_c$ and $M_c$ are the intrinsic and external camera parameters, and $K_p$ and $M_p$ are the intrinsic and external projector parameters, all of which are calculated in the camera calibration process [43]. $z_c$ and $z_p$ are scale factors. By using the parameters of the stereo camera system in Eqs. (5) and (6), the 3D coordinates of the points in the world coordinate system can be thus calculated, forming a complete 3D point cloud model.

## 3. EXPERIMENTAL SETUP AND CHARACTERIZATION

Figure 3(a) shows the optical design diagram of the P4DS imager. The system consists of a 450 nm projector (TENGJU TECHNOLOGY TJ50), an LCTF (with a spectral resolution of 10 nm), and a camera (HIKVISION, MV-CE050-30GM). The 4D imaging process contains two steps: 3D reconstruction and spectra acquisition. In the first step, the wavelength of the LCTF is set to 450 nm, corresponding to the wavelength of the projected light from the projector. In this way, the light projected on the object can pass through the LCTF and be collected by the camera while other wavelengths are blocked. Structured light stripes with different frequencies are projected on the target by the projector, and corresponding images are captured in sequence by the camera after passing through the imaging lens and the LCTF. The sequencing of the projection of light stripes and image acquisition is controlled by a controller, and the process is repeated until images corresponding to all projected structured light stripes have been captured by the camera. The captured images are then used for 3D coordinate reconstruction and the generation of a 3D point cloud model of the measured object in the manner discussed in the previous section. In the second step, the LCTF is set to work in hyperspectral imaging mode by the controller. Light at different wavelengths is passed through the LCTF and imaging lenses and imaged on the camera plane in sequence. The corresponding monochrome images are captured by the camera to form a hyperspectral cube. As the 3D reconstruction and spectra collection share the same camera imaging plane, the two data sets can subsequently directly be fused into a 4D data set without the need for post-processing.
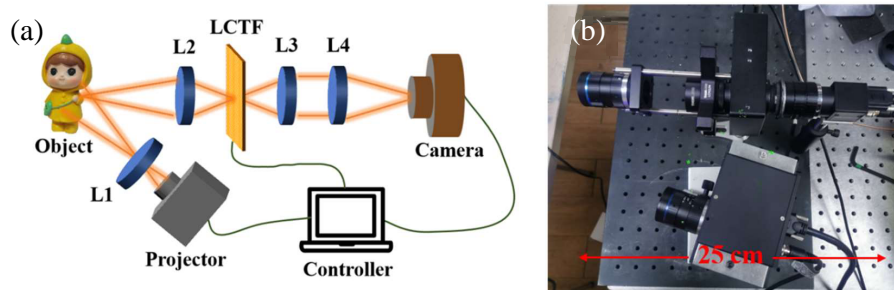


**Figure 3.** (a) The optical diagram and (b) laboratory prototype of the P4DS imager. L1, L2: imaging lens; L3: collimating lens; L4: focusing lens.

Plane fit standard deviation [28] using a flat surface circular plane array board as the reference was used to evaluate the performance of the 3D reconstruction. The ideal reconstruction of the flat board, the best-fitting plane, is a flat plane in which all 3D points are distributed in the same plane. However, in an actual measurement, the reconstructed 3D points will deviate from the best-fitting plane, and the extent of the deviation can be used as a metric of the 3D reconstruction accuracy. Performing a plane fit standard deviation reference calculation, the standard deviation between the measured 3D points and its best-fitting plane is found to be 0.0557 mm, with a maximum deviation calculated to be 0.6306 mm.

## 4. RESULTS

Here we present a set of sample imaging experiments to demonstrate the performance and versatility of the proposed portable 4D snapshot hyperspectral imager. The prototype P4DS imager is used to image a colored figurine, a fresh broccoli and a human face.
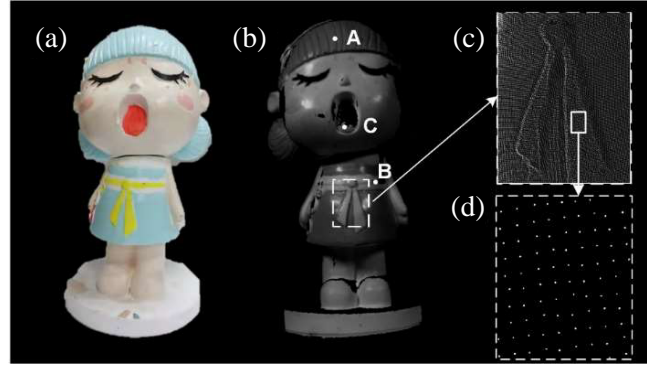
**Figure 4.** (a) Photograph and (b) 3D point cloud model with artificial gray shading of the figurine. (c) Enlargement of the rectangular region indicated in (b). (d) The distribution of the point cloud of the rectangular region indicated in (c).



**Figure 5.** (a) 4D model of the figurine observed at different angles and wavelengths. (b) Normalized reflectance spectra of points indicated in Fig. (b).

## 4.1. 4D Imaging of a Colored Figurine

We first measured a colored figurine to demonstrate the 4D imaging effect and performance of the P4DS imager. Fig. 4(a) shows the figurine under measurement, which has light blue hair and dress, yellow belt, and red tongue. Fig. 4(b) shows its 3D shape model with artificial gray shading, and the enlarged pictures of the indicated rectangular region are shown in Figs. 4(c) and (d). We see that the 3D point cloud is dense and smooth and show well details of the reconstructed model.

Figure 5(a) shows the 4D model of the figurine at different wavelengths and different observation angles. The colors of the 3D point cloud were determined by the chromatic value of the specified wavelength, with the brightness determined by the reflectance intensity. Thus, the brightness of a specific-colored part is the highest at its corresponding wavelengths (red at 650 nm, yellow at 570 nm, blue at 450 nm), which is consistent with the 4D imaging results shown in Fig. 5(a). We note that parts of 3D points cloud are missing in the red tough region, which is because the projected 450 nm blue light is hardly reflected by the surface in red color. This problem can be solved by changing the projection light source at different wavelengths. To display the spectral data in detail, we choose three points A, B, and C located at the hair, belt and tongue regions in Fig. 4(b), and acquire their normalized reflectance spectral curves, which are shown in Fig. 5(b). The characteristics of these spectral curves consist of blue, yellow, and red color properties of those indicated regions.

The results of this experiment demonstrate the high quality 4D imaging obtained by our system, enabling a detailed visualization of spectral signatures at the reconstructed 3D surface model.

## 4.2. 4D Imaging of a Green Plant

A potentially promising application for the proposed system is plant growth monitoring. 3D measurements can provide information about growth state and physical defects, while spectral data can be used for the evaluation of plant quality, maturity, and health state. For instance, chlorophyll content and distribution, indicators of growth and health state of green plants, can be discerned from spectral data measured in the visible bands. Also, in contrast with chemical analysis [44], 4D hyperspectral imaging is a noninvasive and thus nondestructive method, allowing a large number of observations without damaging any plants. To exemplify this, we performed a 4D imaging experiment on fresh broccoli using the P4DS imager.

Figure 6(a) shows the obtained 3D surface model with artificial white shading of the broccoli. We note that the uneven surface and rich texture of the broccoli are well restored and displayed in the 3D reconstruction model, indicating a high spatial resolution of the system. The 3D point cloud is dense and smooth, as shown in the enlarged region. The 4D data of the broccoli model is shown for different wavelengths in Figs. 6(b)–(f). The plant appears brighter at 540 nm compared to other wavelengths, indicating a higher reflectance in the wavelength band around 540 nm.
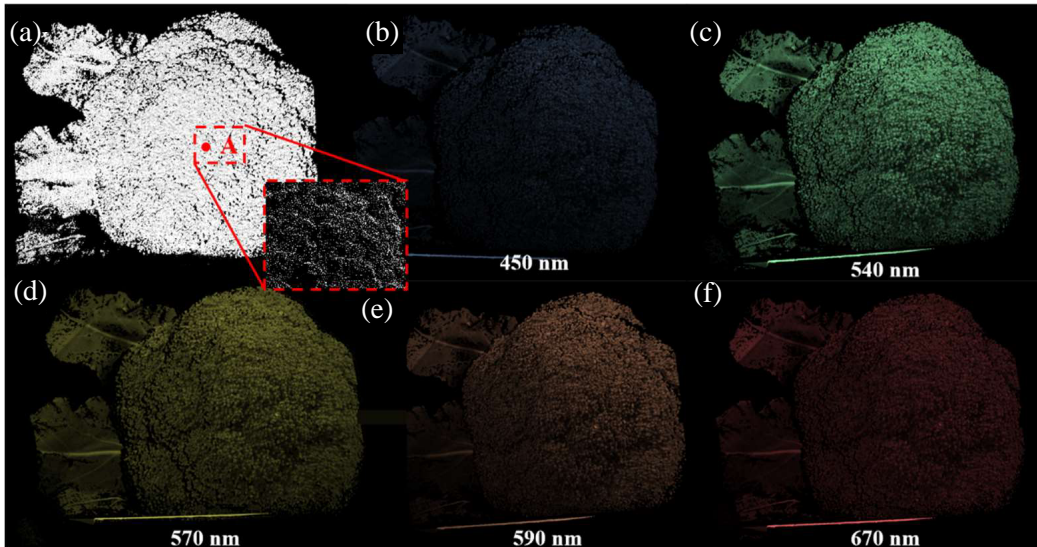


**Figure 6.** (a) 3D surface model of the broccoli using artificial white shading. (b)–(f) 4D broccoli model shown at different wavelengths 450 nm, 540 nm, 570 nm, 590 nm and 670 nm, respectively.

The reconstructed 3D model with the size and depth information is shown in Fig. 7(a), in which color variations are used to represent depth information. The size of the broccoli is found to be 138 mm × 138 mm. Fig. 7(b) shows the normalized reflectance spectrum curve of point A (as indicated in Fig. 7(a)), which has a main reflectance peak at 560 nm and additional absorption peaks at 450 nm and 670 nm, corresponding to the light absorption characteristics of chlorophyll. The normalized reflectance spectrum is calculated by dividing the intensity spectrum of the selected point by the intensity spectrum of a standard whiteboard. In this way, the influence of the light source spectrum is eliminated. To explore the chlorophyll distribution in the broccoli, we define an optical absorption intensity of chlorophyll (OAIC) factor as:

$$OAIC = \frac{\alpha_{670}}{\alpha_{560}} \qquad (7)$$

where $\alpha_\lambda$ is the normalized reflectance at wavelength $\lambda$, and 560 nm and 670 nm are the reflectance and absorption peaks of the normalized reflectance curve, respectively. Fig. 7(c) shows the 4D broccoli model in which the color is set by the OAIC value. The darker the color is, the smaller the OAIC factor is, indicating the stronger optical absorption. The color distribution of the model is uniform, indicating
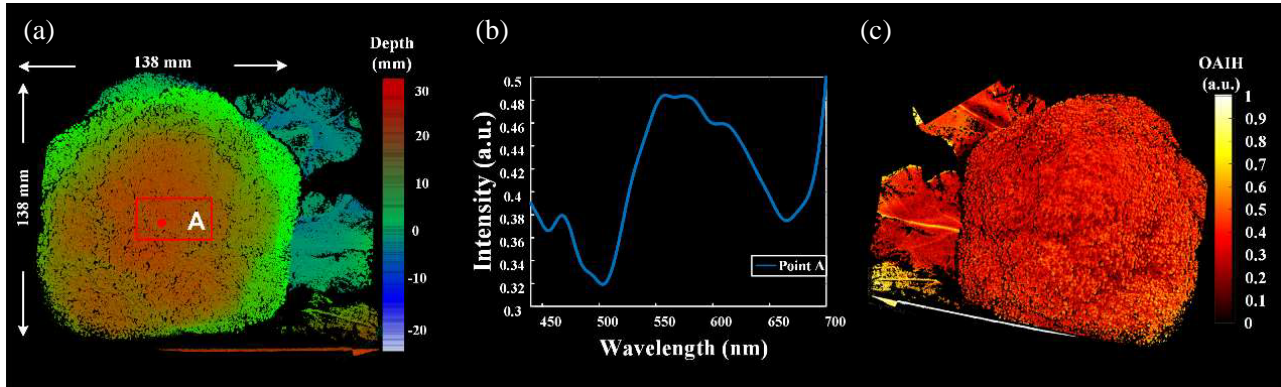
**Figure 7.** (a) 3D surface model of the broccoli with color set by depth information. (b) Normalized spectral curve of point A indicated in (a). (c) 4D broccoli model, in which the color of the 3D points is determined by the OAIC factor.

a uniform chlorophyll distribution in the broccoli. The leaf at the left bottom appears yellowish in Fig. 7(c), indicating a fairly high OAIC and low chlorophyll content, which demonstrates the ability of the P4DS imager to detect senescence (or lack of freshness) in vegetables.

### 4.3. 4D Imaging of a Human Face

Detection and analysis of the health state of facial skin are of interest in medical cosmetology. From a 4D hyperspectral model of a human face, it is possible to observe skin texture and to monitor, e.g., pigmentation, skin redness, scars, and hemoglobin distribution, enabling the possibility of developing customized facial skincare products. Such models also have the potential to be used to evaluate the health or stress situation of subjects.

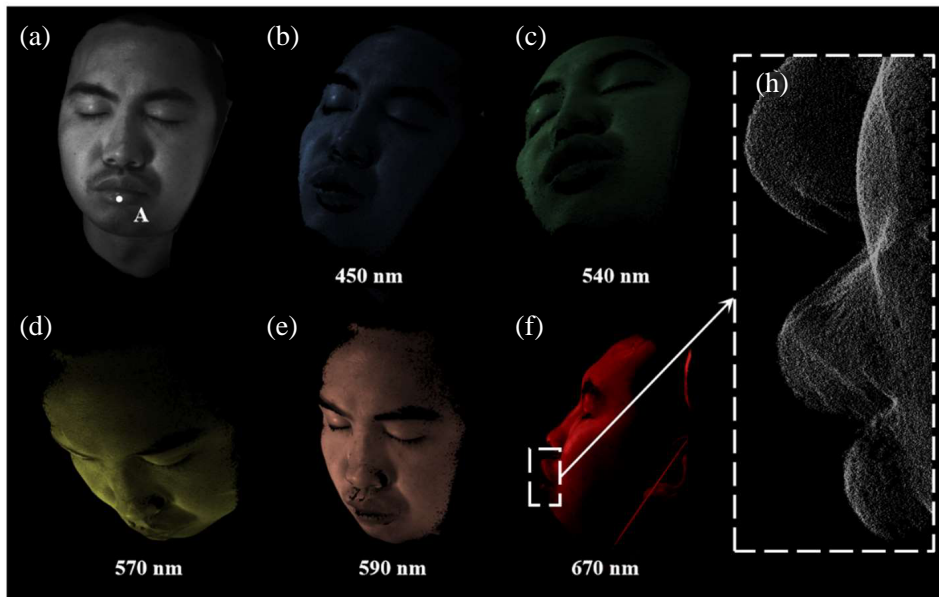Using the P4DS imager, we measured the face of a 26-year-old male subject shown in the



**Figure 8.** (a) 2D photo of the face of the male subject. (b)–(f) 4D face model shown at different wavelengths 450 nm, 540 nm, 570 nm, 590 nm and 670 nm, respectively. (h) Enlarged region of the lips indicated in (f).
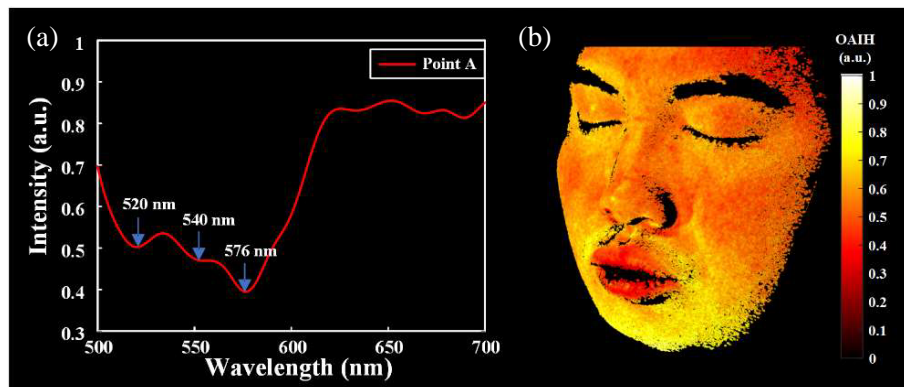
**Figure 9.** (a) Normalized spectral curve of point A indicated in Fig. 8(a). (b) 4D face model, where the color of the 3D points is determined by the OAIH factor.

conventional photograph in Fig. 8(a). The imaging time of one 4D measurement is just less than 1 second, which is conveniently short for the subjects. In such a short time, the subjects are able to remain motionless, and thus the influence of motion on the imaging quality can be greatly reduced. Figs. 8(b)–(f) show the 4D face model at different wavelengths, with an enlarged region of the lip shown in Fig. 8(h).

The normalized reflectance spectrum curve of point A (indicated in Fig. 8(a)) is displayed in Fig. 9(a). The curve has absorption peaks located at 520 nm, 540 nm, and 576 nm, which corresponds to the spectral characteristics of hemoglobin. For quantitative analysis of the hemoglobin distribution on the human face, we define an optical absorption intensity of hemoglobin (OAIH) factor as:

$$OAIH = \frac{\alpha_{576}}{\alpha_{560}} \tag{8}$$

where $\alpha_\lambda$ is the normalized reflectance at wavelength $\lambda$, and 560 nm and 576 nm are the reflectance and absorption peaks of the normalized reflectance curve, respectively. Fig. 9(b) shows the 4D face model of hemoglobin absorption characteristics, with the color set by the value of the OAIH factor, and the brightness is negatively associated with the intensity of light absorption. The red color is the darkest in the lip region, indicating that the lip has the highest content of hemoglobin, followed by the nose and the cheek, which match the distribution of blood vessels in the human face [45].

## 5. CONCLUSION

We have presented a portable 4D snapshot hyperspectral imager (P4DS imager) that can simultaneously acquire 3D spatial and spectral information of measured objects. The key components of the P4DS imager are a projector, a liquid crystal tunable filter (LCTF), and a camera. In the 3D measurement mode, structured light stripes are projected on the object by the projector. The images captured by the camera are then used to construct a 3D point cloud of the object. In the hyperspectral imaging mode, monochrome images of the object at different wavelengths selected by the LCTF are collected by the camera to form a hyperspectral cube. Since the camera imaging plane is the same in both measurement modes, the spatial and spectral data can directly be fused into a full 4D data set without post-processing of the measurement data. The system shows excellent performance, with a spatial and spectral resolutions of 55.7 μm and 10 nm, respectively, and a total 4D imaging time of about 0.8 s for one measurement. We have presented imaging experiments of a colored figurine, a green plant and a human face to demonstrate the efficiency and applicability of the system. The distribution of chlorophyll in the broccoli and hemoglobin in the human face could be qualitatively analyzed. The results demonstrate that the system can be used to qualitatively detect and analyze substance distribution and properties of a 3D surface.

Compared with previously published work, our proposed 4D snapshot hyperspectral imager has the advantages of being portable, cost-effective, high-speed, and having a performance sufficient for a large

range of applications. As such, it is a suitable design for commercialization of 4D imaging to be used in a variety of applications, such as digital documentation of cultural relics and art, precision agriculture, and dermatology.

## ACKNOWLEDGMENT

## REFERENCES

1. Li, Q. L., Y. T. Wang, H. Y. Liu, X. F. He, D. R. Xu, J. B. Wang, and F. M. Guo, "Leukocyte cells identification and quantitative morphometry based on molecular hyperspectral imaging technology," *Computerized Medical Imaging and Graphics*, Vol. 38, No. 3, 171–178, 2014.
2. Yao, X., S. Li, and S. L. He, "Dual-mode hyperspectral bio-imager with a conjugated camera for quick object-selection and focusing," *Progress In Electromagnetics Research*, Vol. 168, 133–143, 2020.
3. Liu, X. M., Z. Q. Jiang, T. C. Wang, F. H. Cai, and D. Wang, "Fast hyperspectral imager driven by a low-cost and compact galvo-mirror," *Optik*, Vol. 224, 165716, 2020.
4. Wu, D. and D. W. Sun, "Advanced applications of hyperspectral imaging technology for food quality and safety analysis and assessment: A review — Part I: Fundamentals," *Innovative Food Sci. Emerg. Technol.*, Vol. 19, 1–14, 2013.
5. Zdoan, G., X. H. Lin, and D. W. Sun, "Rapid and noninvasive sensory analyses of food products by hyperspectral imaging: Recent application developments," *Trends in Food Science & Technology*, Vol. 111, 151–165, 2021.
6. Ramakrishnan, D. and R. Bharti, "Hyperspectral remote sensing and geological applications," *Current Science*, Vol. 108, No. 5, 879–891, 2015.
7. Sun, Y., Y. J. Zhao, K. Qin, J. T. Nie, and H. B. Li, "Geological application of HySpex ground hyperspectral remote sensing in gold and uranium ore deposits," *Asia-Pacific Energy Equipment Engineering Research Conference (AP3ER)*, Vol. 9, 392–395, 2015.
8. Courtenay, L. A., D. Gonzalez-Aguilera, S. Laguela, S. del Pozo, C. Ruiz-Mendez, I. Barbero-Garcia, C. Roman-Curto, J. Canueto, C. Santos-Duran, M. E. Cardenoso-Alvarez, M. Roncero-Riesco, D. Hernandez-Lopez, D. Guerrero-Sevilla, and P. Rodriguez-Gonzalvez, "Hyperspectral imaging and robust statistics in non-melanoma skin cancer analysis," *Biomed. Opt. Express*, Vol. 12, No. 8, 5107–5127, 2021.
9. Dicker, D. T., J. Lerner, P. Van Belle, S. F. Barth, D. Guerry, M. Herlyn, and W. S. El-Deiry, "Differentiation of normal skin and melanoma using high resolution hyperspectral imaging," *Cancer Biology & Therapy*, Vol. 5, No. 8, 1033–1038, 2006.
10. Manley, M., "Near-infrared spectroscopy and hyperspectral imaging: Non-destructive analysis of biological materials," *Chem. Soc. Rev.*, Vol. 43, No. 24, 8200–8214, 2014.
11. Studer, V., J. Bobin, M. Chahid, H. S. Mousavi, E. Candes, and M. Dahan, "Compressive fluorescence microscopy for biological and hyperspectral imaging," *Proceedings of the National Academy of Sciences of the United States of America*, Vol. 109, No. 26, E1679–E1687, 2012.
12. Yang, Q. L., B. Niu, S. Q. Gu, J. G. Ma, C. M. Zhao, Q. Chen, D. H. Guo, X. J. Deng, Y. A. Yu, and F. Zhang, "Rapid detection of nonprotein nitrogen adulterants in milk powder using point-scan raman hyperspectral imaging technology," *ACS Omega*, Vol. 7, No. 2, 2064–2073, 2022.
13. Yao, X. L., F. H. Cai, P. Y. Zhu, H. X. Fang, J. W. Li, and S. L. He, "Non-invasive and rapid pH monitoring for meat quality assessment using a low-cost portable hyperspectral scanner," *Meat Sci.*, Vol. 152, 73–80, 2019.

14. Gomez-Sanchis, J., J. Blasco, E. Soria-Olivas, D. Lorente, P. Escandell-Montero, J. M. Martinez-Martinez, M. Martinez-Sober, and N. Aleixos, "Hyperspectral LCTF-based system for classification of decay in mandarins caused by Penicilliumdigitatum and Penicilliumitalicum using the most relevant bands and non-linear classifiers," *Postharvest Biol. Technol.*, Vol. 82, 76–86, 2013.

15. Abdlaty, R., J. Orepoulos, P. Sinclair, R. Berman, and Q. Y. Fang, "High throughput AOTF hyperspectral imager for randomly polarized light," *Photonics*, Vol. 5, No. 1, 3, 2018.

16. Gat, N., "Imaging spectroscopy using tunable filters: A review," *Conference on Wavelet Applications VII*, Vol. 4056, 50–64, 2000.

17. Wang, X., Y. Zhang, X. Ma, T. Xu, and G. R. Arce, "Compressive spectral imaging system based on liquid crystal tunable filter," *Opt. Express*, 26, No. 19, 25226–25243, 2018.

18. Gebhart, S. C., R. C. Thompson, and A. Mahadevan-Jansen, "Liquid-crystal tunable filter spectral imaging for brain tumor demarcation," *Appl. Opt.*, 46, No. 10, 1896–1910, 2007.

19. Nalpantidis, L., G. C. Sirakoulis, and A. Gasteratos, "Review of stereo vision algorithms: From software to hardware," *Int. J. Optomechatronics*, Vol. 2, No. 4, 435–462, 2008.

20. Dhond, U. R. and J. K. Aggarwal, "Structure from stereo — A review," *IEEE Transactions on Systems Man and Cybernetics*, Vol. 19, No. 6, 1489–1510, 1989.

21. Zhang, S., "High-speed 3D shape measurement with structured light methods: A review," *Opt. Lasers Eng.*, Vol. 106, 119–131, 2018.

22. Hyun, J. S., G. T. C. Chiu, and S. Zhang, "High-speed and high-accuracy 3D surface measurement using a mechanical projector," *Opt. Express*, Vol. 26, No. 2, 1474–1487, 2018.

23. Foix, S., G. Alenya, and C. Torras, "Lock-in Time-of-Flight (ToF) cameras: A survey," *IEEE Sens. J.*, Vol. 11, No. 9, 1917–1926, 2011.

24. Luo, L. Q., X. Chen, Z. P. Xu, S. Li, Y. R. Sun, and S. L. He, "A parameter-free calibration process for a scheimpflug LIDAR for volumetric profiling," *Progress In Electromagnetics Research*, Vol. 169, 117–127, 2020.

25. Zhong, K., Z. W. Li, X. H. Zhou, Y. F. Li, Y. S. Shi, and C. J. Wang, "Enhanced phase measurement profilometry for industrial 3D inspection automation," *Int. J. Adv. Manuf. Technol.*, Vol. 76, Nos. 9–12, 1563–1574, 2015.

26. Caudullo, P. T., "3D laser scanning: technology at the service of the protection of cultural heritage," *Archeomatica-Tecnologie Per I Beni Culturali*, Vol. 11, No. 3, 6–9, 2020.

27. Jahanshahi, M. R. and S. F. Masri, "Adaptive vision-based crack detection using 3D scene reconstruction for condition assessment of structures," *Autom. Constr.*, Vol. 22, 567–576, 2012.

28. Peng, H. C., Z. C. Ruan, F. H. Long, J. H. Simpson, and E. W. Myers, "V3D enables real-time 3D visualization and quantitative analysis of large-scale biological image data sets," *Nat. Biotechnol.*, Vol. 28, No. 4, 348–375, 2010.

29. Cai, F. H., T. C. Wang, J. J. Wu, and X. Y. Zhang, "Handheld four-dimensional optical sensor," *Optik*, Vol. 203, 164001, 2020.

30. Aasen, H., A. Burkart, A. Bolten, and G. Bareth, "Generating 3D hyperspectral information with lightweight UAV snapshot cameras for vegetation monitoring: From camera calibration to quality assurance," *ISPRS J. Photogramm. Remote Sens.*, Vol. 108, 245–259, 2015.

31. Zhao, H. J., Z. Y. Wang, G. R. Jia, X. D. Li, and Y. Zhang, "Field imaging system for hyperspectral data, 3D structural data and panchromatic image data measurement based on acousto-optic tunable filter," *Opt. Express*, Vol. 26, No. 13, 17717–17730, 2018.

32. Zhao, H. J., L. B. Xu, S. G. Shi, H. Z. Jiang, and D. Chen, "A high throughput integrated hyperspectral imaging and 3D measurement system," *Sensors*, Vol. 18, No. 4, 1608, 2018.

33. Heist, S., C. Zhang, K. Reichwald, P. Kuhmstedt, G. Notni, and A. Tuennermann, "5D hyperspectral imaging: Fast and accurate measurement of surface shape and spectral characteristics using structured light," *Opt. Express*, Vol. 26, No. 18, 23366–23379, 2018.

34. Luo, J., S. Li, E. Forsberg, and S. L. He, "4D surface shape measurement system with high spectral resolution and great depth accuracy," *Opt. Express*, Vol. 29, No. 9, 13048–13070, 2021.

35. Ivorra, E., S. Verdu, A. J. Sanchez, R. Grau, and J. M. Barat, "Predicting gilthead sea bream (Sparus aurata) freshness by a novel combined technique of 3D imaging and SW-NIR spectral analysis," *Sensors*, Vol. 16, No. 10, 1735, 2016.

36. Kim, M. H., H. Rushmeier, J. Dorsey, T. A. Harvey, R. O. Prum, D. S. Kittle, and D. J. Brady, "3D imaging spectroscopy for measuring hyperspectral patterns on solid objects," *ACM Trans. Graphics*, Vol. 31, No. 4, 1–11, 2012.

37. Chen, B. W., S. Shi, J. Sun, W. Gong, J. Yang, L. Du, K. H. Guo, B. H. Wang, and B. W. Chen, "Hyperspectral lidar point cloud segmentation based on geometric and spectral information," *Opt. Express*, Vol. 27, No. 17, 24043–24059, 2019.

38. Li, J. Q., Y. Zheng, L. L. Liu, and B. W. Li, "4D line-scan hyperspectral imaging," *Opt. Express*, Vol. 29, No. 21, 34835–34849, 2021.

39. Beeckman, J., K. Neyts, and P. J. M. Vanbrabant, "Liquid-crystal photonic applications," *Opt. Eng.*, Vol. 50, No. 8, 081202, 2011.

40. Aharon, O. and I. Abdulhalim, "Tunable optical filter having a large dynamic range," *Opt. Lett.*, Vol. 34, No. 14, 2114–2116, 2009.

41. Zuo, C., S. J. Feng, L. Huang, T. Y. Tao, W. Yin, and Q. Chen, "Phase shifting algorithms for fringe projection profilometry: A review," *Opt. Lasers Eng.*, Vol. 109, 23–59, 2018.

42. Reich, C., R. Ritter, and J. Thesing, "White light heterodyne principle for 3D-measurement," *Proc. SPIE*, Vol. 3100, No. 1, 236–244, 1997.

43. Li, Z., Y. Shi, C. Wang, and Y. Wang, "Accurate calibration method for a structured light system," *Opt. Eng.*, Vol. 47, No. 5, 053604, 2008.

44. Bajguz, A. and A. Tretyn, "The chemical characteristic and distribution of brassinosteroids in plants," *Phytochemistry*, Vol. 62, No. 7, 1027–1046, 2003.

45. Pilsl, U., F. Anderhuber, and S. Neugebauer, "The facial artery-the main blood vessel for the anterior face?," *Dermatologic Surgery*, Vol. 42, No. 2, 203–208, 2016.